

# SPECTRAL DIFFUSION MODELS ON THE SPHERE

PIERPAOLO BRUTTI, CLAUDIO DURASTANTI, AND FRANCESCO MARI

**ABSTRACT.** Diffusion models provide a principled framework for generative modeling via stochastic differential equations and time-reversed dynamics. Extending spectral diffusion approaches to spherical data, however, raises nontrivial geometric and stochastic issues that are absent in the Euclidean setting.

In this work, we develop a diffusion modeling framework defined directly on finite-dimensional spherical harmonic representations of real-valued functions on the sphere. We show that the spherical discrete Fourier transform maps spatial Brownian motion to a constrained Gaussian process in the frequency domain with deterministic, generally non-isotropic covariance. This induces modified forward and reverse-time stochastic differential equations in the spectral domain.

As a consequence, spatial and spectral score matching objectives are no longer equivalent, even in the band-limited setting, and the frequency-domain formulation introduces a geometry-dependent inductive bias. We derive the corresponding diffusion equations and characterize the induced noise covariance.

**Keywords:** Diffusion models, Score-based generative modeling, Spherical harmonics, Spectral diffusion, Spherical data, Stochastic differential equations

**MSC Classification:** 60H10, 42C10, 62H11

## 1. INTRODUCTION

Deep generative models aim to learn complex, high-dimensional probability distributions by exploiting inductive biases encoded in neural network architectures. Over the past decade, such models have achieved remarkable empirical success across a wide range of domains, including image synthesis [21], audio generation [23], and natural language processing [13], as well as applications in the natural sciences such as protein structure design [41], molecular and drug discovery [42], and materials modeling [43]. Within this broad landscape, diffusion models [19, 20, 33, 36] have emerged as a particularly powerful and flexible class of generative methods, distinguished by their formulation in terms of stochastic differential equations and time-reversed stochastic dynamics.

This continuous-time formulation has recently received rigorous treatment in the mathematical literature, where score-based generative models are analyzed explicitly as stochastic differential equations and their time reversals, including via Malliavin-calculus-based approaches [29, 38]. From a probabilistic viewpoint, reverse-time diffusion dynamics can be interpreted

through the theory of conditioned diffusions, whose structural and asymptotic properties have been studied in depth in stochastic analysis [3].

Within this framework, diffusion models construct generative mechanisms by defining a forward-time stochastic process that gradually perturbs the data distribution into a simple reference measure, typically a standard Gaussian. Sampling is then achieved by simulating the corresponding reverse-time dynamics, yielding stable training procedures, principled likelihood-based objectives, and state-of-the-art sample quality in both unconditional and conditional settings [12, 31].

Among the various formulations of diffusion models, score-based generative modeling via stochastic differential equations (SDEs) [36] provides a unified and mathematically transparent framework. In this setting, a forward SDE progressively transforms the data distribution toward a tractable terminal density  $p_T$ , while generation is obtained by simulating the associated time-reversed SDE, whose drift depends explicitly on the score function  $\nabla_x \log p_t(x)$ . This continuous-time formulation establishes a clear connection between diffusion models, stochastic analysis, and partial differential equations, and highlights the central role played by the geometry of the underlying data space and the covariance structure of the driving noise, which together determine the form of the reverse-time dynamics.

Crucially, this perspective reveals that diffusion models are not invariant to the choice of representation. Changing the representation space alters the stochastic dynamics, modifies the structure of the noise, and affects the form of the reverse-time drift. From a probabilistic standpoint, this implies that different representations induce different geometric and statistical properties on the diffusion process, which in turn influence both training dynamics and generative performance. The influence of geometry on diffusion dynamics has also been highlighted in recent work on diffusion processes evolving on structured and non-Euclidean spaces, emphasizing how the underlying geometry shapes stochastic behavior [14].

While diffusion models were originally developed for data defined on Euclidean grids, such as images and audio waveforms, there is growing interest in extending these methods to structured data domains where representation plays a fundamental role. Time series provide a canonical example: their temporal dependencies and multiscale structure are often more naturally expressed in the frequency domain, where long-range correlations can be partially decorrelated and global structure becomes explicit. Recent work has shown that diffusion models defined directly in the frequency domain for time series are theoretically equivalent to their time-domain counterparts in terms of score matching objectives, while empirically exhibiting improved modeling of temporal dependencies and global features [10]. These results indicate that spectral diffusion is not merely a reparameterization, but induces a distinct stochastic structure and inductive bias.

However, extending spectral diffusion frameworks from Euclidean or temporal settings to spherical domains is nontrivial. In contrast to the Euclidean

Fourier transform, the spherical harmonic transform of real-valued signals imposes conjugate symmetry constraints and, when combined with discrete quadrature schemes, maps standard Brownian motion in the spatial domain to a correlated process in the spectral domain. As a consequence, the driving noise in frequency space is no longer isotropic, and the associated reverse-time dynamics involve non-diagonal covariance structures. These features fundamentally alter the form of the diffusion SDEs and the corresponding score matching objectives. They must therefore be explicitly accounted for in any principled spherical spectral diffusion framework. Related work has considered score-based diffusion models defined intrinsically on Riemannian manifolds (see, for example, [11]); in contrast, the present work does not construct an intrinsic diffusion on  $\mathbb{S}^2$ , but instead exploits a finite-dimensional spherical harmonic representation in which geometric structure is encoded through spectral constraints and noise covariance.

From a probabilistic standpoint, spectral representations for stochastic processes on the sphere are well established. In particular, spherical time series models, including autoregressive and moving-average (ARMA)-type constructions, have been studied via spherical harmonic decompositions, where stationarity and dependence structures are naturally characterized in the frequency domain [6, 5]. These works demonstrate that harmonic analysis provides a mathematically tractable framework for defining and analyzing stochastic dynamics on spherical domains. In contrast, the present work is concerned with intrinsically nonstationary diffusion processes arising from score-based generative modeling, and with the formulation of forward and reverse-time SDEs directly in the spherical spectral domain.

Many important datasets are naturally defined on spherical domains. Examples include full-sky cosmological observations such as cosmic microwave background and large-scale structure maps [7, 30], global climate and Earth observation fields [8, 39], molecular surface representations in computational chemistry [26, 40], and omnidirectional visual data captured by  $360^\circ$  cameras [9, 25]. For such data, spherical harmonics provide a canonical spectral representation: as eigenfunctions of the Laplace–Beltrami operator on the sphere, they form an orthonormal basis of  $L^2(\mathbb{S}^2)$  and naturally decompose functions into scale-dependent modes that respect the intrinsic geometry and rotational symmetries of the sphere.

Despite the success of spectral diffusion models for Euclidean and sequential data, diffusion processes defined on spherical domains remain comparatively unexplored. In particular, a systematic formulation of score-based diffusion directly in the spherical harmonic domain—accounting for symmetry constraints, induced noise covariance, and the structure of reverse-time dynamics—is largely missing from the literature. From a stochastic analysis perspective, this raises the question of whether diffusion processes on the sphere can be equivalently and effectively formulated in the frequency domain, and how the geometry of  $\mathbb{S}^2$  manifests itself in the resulting stochastic dynamics.

In this work, we address this question by proposing a diffusion modeling framework defined directly in the space of spherical harmonic coefficients. By formulating both the forward and reverse diffusion processes in the spectral domain, we exploit the intrinsic geometry of the sphere and introduce a structured, scale-aware inductive bias. We show that the spherical Fourier transform maps standard Brownian motion in the spatial domain to a constrained stochastic process in the frequency domain, which we characterize as a *spherical mirrored Brownian motion* with nontrivial covariance structure. Within this framework, we derive the corresponding forward and reverse-time SDEs, provide a precise description of the induced noise covariance, and establish the relationship between score matching objectives in the spatial and spectral domains.

The resulting framework is fully compatible with the score-based SDE formalism, while naturally encoding spherical geometry and symmetry constraints. It provides a principled foundation for generative modeling of spherical data, with potential applications in cosmology, climate science, computational chemistry, and computer graphics.

Several natural extensions of the present framework merit future investigation. While all constructions in this work are finite-dimensional with a fixed band limit  $L$ , an important open question concerns the asymptotic behavior of the spectral diffusion process as  $L \rightarrow \infty$ , and its relationship to diffusions defined intrinsically on  $L^2(\mathbb{S}^2)$ . Related directions include the study of robustness with respect to the choice of spherical sampling and quadrature schemes, as well as extensions to anisotropic noise, other compact homogeneous spaces, or alternative spectral representations.

The remainder of the paper is organized as follows. Section 2 reviews score-based diffusion models and the elements of harmonic analysis required to define diffusion processes on  $\mathbb{S}^2$ . Section 3 presents our main contribution, developing a matrix-based formulation of the spherical discrete Fourier transform and deriving the associated forward and reverse diffusion SDEs in the frequency domain, together with a detailed characterization of the induced noise structure. Section 4 provides illustrative numerical experiments on synthetic, band-limited spherical signals, designed to complement the theoretical analysis and highlight the geometric and stochastic effects induced by the spectral formulation. Section 5 contains all proofs.

## 2. BACKGROUND

To establish the foundations of our spectral diffusion framework on the sphere, we first review score-based generative modeling in Euclidean spaces (see, among others, [20, 34]), and then introduce the elements of harmonic analysis required to extend these ideas to spherical domains (cf. [27, 2]). Throughout the paper, vectors in Euclidean space are denoted by bold lowercase letters  $\mathbf{x} \in \mathbb{R}^n$ , while complex-valued vectors are written  $\mathbf{z} \in \mathbb{C}^d$ , with

$\Re[\mathbf{z}]$  and  $\Im[\mathbf{z}]$  denoting their real and imaginary parts. Time-dependent stochastic processes are written  $\mathbf{x}(t)$ , with  $p_t$  denoting their marginal densities, and  $\mathbf{w}$  standard Brownian motion.

**2.1. Score-Based Generative Modeling in Euclidean Space.** Score-based diffusion models construct generative mechanisms by coupling stochastic dynamics with learned gradient fields of evolving probability densities.

The central idea is to define a forward-time stochastic process that gradually transforms the data distribution into a simple reference measure, and then to invert this process by simulating the corresponding reverse-time dynamics.

**Forward Diffusion.** Let  $\mathbf{x} \in \mathbb{R}^n$  denote data drawn from an unknown density  $p_{\text{data}}$ .

In continuous-time diffusion models, the forward process is defined by the stochastic differential equation

$$d\mathbf{x} = \mathbf{f}(\mathbf{x}, t)dt + \mathbf{G}(t)d\mathbf{w}, \quad (1)$$

where  $\mathbf{f}(\mathbf{x}, t)$  is a drift term and  $\mathbf{G}(t)$  a time-dependent diffusion matrix.

The marginal density of  $\mathbf{x}(t)$  is denoted by  $p_t$ , with initial condition  $p_0 = p_{\text{data}}$ . The functions  $\mathbf{f}$  and  $\mathbf{G}$  are chosen so that, as  $t \rightarrow T$ , the distribution  $p_t$  converges to a tractable reference density  $p_T$ , typically a standard Gaussian.

**Reverse Diffusion.** Generation is achieved by reversing the forward diffusion. Starting from samples drawn from  $p_T$ , one simulates a reverse-time stochastic process whose marginals evolve toward  $p_0$ . As shown in the classical work [1], the reverse-time dynamics satisfy

$$d\mathbf{x} = \mathbf{b}(\mathbf{x}, t)dt + \mathbf{G}(t)d\hat{\mathbf{w}}, \quad (2)$$

where time flows from  $T$  to 0,  $\hat{\mathbf{w}}$  is Brownian motion in reverse time, and

$$\mathbf{b}(\mathbf{x}, t) = \mathbf{f}(\mathbf{x}, t) - \mathbf{G}(t)\mathbf{G}(t)^T \nabla_{\mathbf{x}} \log p_t(\mathbf{x}).$$

The reverse drift depends explicitly on the score function  $\nabla_{\mathbf{x}} \log p_t(\mathbf{x})$ . Once this score is known or well approximated, the reverse SDE can be simulated to generate samples from the data distribution.

**Score Estimation.** Since the intermediate densities  $p_t$  are unknown, score-based diffusion models learn an approximation of the score function directly from data. This is achieved via denoising score matching [20, 34], by training a neural network  $s_{\theta}(\mathbf{x}, t)$  to minimize

$$\theta^* = \underset{\theta}{\operatorname{argmin}} \mathbb{E}_t \left[ \lambda(t) \mathbb{E}_{\mathbf{x}(0)} \mathbb{E}_{\mathbf{x}(t) \mid \mathbf{x}(0)} \| s_{\theta}(\mathbf{x}(t), t) - \nabla_{\mathbf{x}(t)} \log p_{0,t}(\mathbf{x}(t) \mid \mathbf{x}(0)) \|_2^2 \right], \quad (3)$$

where  $p_{0,t}$  denotes the transition kernel of the forward SDE. Under mild regularity assumptions and sufficient model capacity, the minimizer recovers the true score almost everywhere.

This perspective highlights that diffusion models are fundamentally constrained by the geometry and representation of the data space, especially outside the Euclidean case.

**2.2. Harmonic Analysis on the Sphere.** Spherical harmonics provide the natural analogue of the Fourier basis for functions defined on the unit sphere  $\mathbb{S}^2$ . They form an orthonormal basis of  $L^2(\mathbb{S}^2)$ , allowing spherical data to be represented through frequency components indexed by degree and order.

This spectral decomposition is central to both theoretical analysis and practical modeling, as it separates global and local features, enables the construction of rotationally invariant operators, and supports scale-dependent regularization and stochastic dynamics.

Harmonic representations on the sphere have long played a fundamental role in statistical inference for spherical data, with applications ranging from spectral estimation in Gaussian models [17] to spherical time series and functional autoregressions [6].

From the perspective of generative modeling, these properties make spherical harmonics a natural vehicle for transferring diffusion-based methodologies from Euclidean spaces to spherical domains, while respecting intrinsic geometry and rotational symmetries.

**Spherical Harmonics.** Let  $L^2(\mathbb{S}^2)$  denote the space of square-integrable functions on the unit sphere, equipped with the inner product

$$\langle f, g \rangle = \int_{\mathbb{S}^2} f(\theta, \phi) g^*(\theta, \phi) d\Omega(\theta, \phi), \quad d\Omega = \sin \theta d\theta d\phi,$$

where  $(\theta, \phi) \in [0, \pi] \times [0, 2\pi]$  denote colatitude and longitude respectively.

An orthonormal basis of  $L^2(\mathbb{S}^2)$  is given by the spherical harmonics

$$\{Y_{\ell,m}(\theta, \phi) : \ell \in \mathbb{N}_0, m = -\ell, \dots, \ell\},$$

indexed by degree  $\ell \in \mathbb{N}_0$  and order  $|m| \leq \ell$ , defined as

$$Y_{\ell,m}(\theta, \phi) = \sqrt{\frac{\ell+1}{4\pi} \frac{(\ell-m)!}{(\ell+m)!}} P_{\ell,m}(\cos \theta) e^{im\phi}, \quad m \geq 0,$$

with extension to  $m < 0$  via conjugate symmetry. Here  $P_{\ell,m}$  are the associated Legendre functions [37].

Any  $f \in L^2(\mathbb{S}^2)$  admits the spherical harmonic expansion

$$f(\theta, \phi) = \sum_{\ell=0}^{\infty} \sum_{m=-\ell}^{\ell} a_{\ell,m} Y_{\ell,m}(\theta, \phi), \quad a_{\ell,m} = \langle f, Y_{\ell,m} \rangle.$$

The coefficients  $\{a_{\ell,m} : \ell \in \mathbb{N}_0, m = -\ell, \dots, \ell\}$  encode angular frequency content, with  $\ell$  controlling spatial scale and  $m$  azimuthal oscillations.

The following properties are particularly relevant for spectral modeling:

- *Orthonormality:*  $\langle Y_{\ell,m}, Y_{\ell',m'} \rangle = \delta_{\ell\ell'} \delta_{mm'}$ .
- *Conjugate symmetry:*  $Y_{\ell,-m} = (-1)^m Y_{\ell,m}^*$ , implying  $a_{\ell,-m} = (-1)^m a_{\ell,m}^*$ .
- *Eigenfunction property:*  $\Delta_{\mathbb{S}^2} Y_{\ell,m} = -\ell(\ell+1) Y_{\ell,m}$ .

Band-Limited Functions and Sampling. In practice, we work with band-limited functions for which  $a_{\ell,m} = 0$  for  $\ell \geq L$ . Such functions admit exact reconstruction from finitely many samples using appropriate quadrature schemes [15].

Throughout this work, we adopt a uniform sampling scheme following [28], which provides explicit sampling nodes and quadrature weights enabling exact analysis and synthesis of band-limited functions. More in detail, for a function band-limited at degree  $L$ , exact recovery is possible from a finite set of samples. Following [28], we introduce uniform sampling nodes in colatitude and longitude,

$$\theta_j = \frac{(2j+1)\pi}{4L}, \quad j = 0, \dots, 2L-1, \quad \phi_k = \frac{2\pi k}{2L-1}, \quad k = 0, \dots, 2L-2,$$

corresponding to evenly spaced points in colatitude and longitude, respectively.

To account for the spherical integration measure, we associate quadrature weights

$$q_j^{(L)} = \frac{2}{L} \sin \theta_j \sum_{\ell=0}^{L-1} \frac{1}{2\ell+1} \sin((2\ell+1)\theta_j),$$

which ensure exact integration of spherical harmonics of degree  $\ell < L$ .

The resulting analysis formula recovers the harmonic coefficients exactly,

$$\hat{a}_{\ell,m} = \frac{2\pi}{2L-1} \sum_{j=0}^{2L-1} \sum_{k=0}^{2L-2} q_j^{(L)} f(\theta_j, \phi_k) Y_{\ell,m}^*(\theta_j, \phi_k), \quad \ell < L, \quad (4)$$

while the corresponding *synthesis formula* reconstructs the band-limited function on the grid,

$$f(\theta_j, \phi_k) = \sum_{\ell=0}^{L-1} \sum_{m=-\ell}^{\ell} \hat{a}_{\ell,m} Y_{\ell,m}(\theta_j, \phi_k). \quad (5)$$

This exact quadrature scheme underlies practical spherical Fourier transforms and discrete spectral methods, and provides the computational basis for probabilistic modeling in the harmonic domain.

*Remark 2.1.* Throughout this section we adopt the equiangular sampling grid of [28], which admits exact quadrature for  $L$ -band-limited functions and leads to a particularly simple Kronecker structure for the weight matrix  $Q$ . This choice is made for notational and computational convenience only. All results extend to any spherical sampling scheme admitting exact quadrature for  $L$ -band-limited functions, such as Gauss–Legendre or related schemes [24], provided the corresponding spherical harmonics matrix  $Y$  and weight matrix  $Q$  are defined accordingly. In all cases, it is essential to balance the number of sampling points with the bandwidth  $L$  to avoid aliasing effects [16, 18]. The diffusion formalism developed below depends only on

the linearity of the spherical DFT and on the induced covariance structure of the transformed noise.

**Probability Densities in the Spectral Domain.** To extend diffusion models to the spectral domain, we define a probability density over the complex-valued spherical harmonic coefficients  $\hat{a}_{\ell,m} \in \mathbb{C}$ . These coefficients are collected in  $\hat{\mathbf{a}} \in \mathbb{C}^{\hat{d}_X}$ , where

$$\hat{d}_X = \sum_{\ell=0}^{L-1} (2\ell + 1) = L^2,$$

counts the total number of independent coefficients. Following standard treatments of complex random vectors [32], we can write the score in terms of real and imaginary parts:

$$\hat{\mathbf{s}}(\hat{\mathbf{a}}) := \nabla_{\Re[\hat{\mathbf{a}}]} \log \hat{p}(\hat{\mathbf{a}}) + i \nabla_{\Im[\hat{\mathbf{a}}]} \log \hat{p}(\hat{\mathbf{a}}),$$

with  $\Re[\cdot]$  and  $\Im[\cdot]$  denoting the real and imaginary components. This allows treating complex coefficients as structured real vectors, suitable for score-based methods in the spectral domain.

The spherical harmonic coefficients satisfy the Hermitian conjugate symmetry

$$\hat{a}_{\ell,m} = (-1)^m \hat{a}_{\ell,-m}^*, \quad 0 < \ell < L, \quad |m| < \ell,$$

ensuring that the reconstructed spatial function  $f(\theta, \phi)$  is real-valued. Not all coefficients are independent: the admissible set forms a linear subspace (equivalently, a lower-dimensional embedded submanifold) of  $\mathbb{C}^{\hat{d}_X}$ , and the score function must respect the mirrored symmetry

$$\hat{\mathbf{s}}_{\ell,m} = (-1)^m \hat{\mathbf{s}}_{\ell,-m}^*.$$

This constraint guarantees that the stochastic dynamics of the spectral diffusion process preserve the reality of the underlying spatial function. By working directly with these constrained coefficients, both forward and reverse diffusions can be defined in the harmonic domain. This naturally encodes the sphere's geometry and symmetries while retaining all information needed for exact reconstruction. This formulation underpins the spectral diffusion framework developed throughout this work.

These symmetry constraints will play a crucial role in determining the covariance structure of the driving noise in the spectral diffusion SDEs derived in Section 3.

### 3. DIFFUSION MODELS IN THE FREQUENCY DOMAIN FOR SPHERICAL DATA

In the previous section, we reviewed the score-based diffusion framework in Euclidean spaces and recalled the elements of harmonic analysis required to represent functions on the sphere. We now specialize to real-valued functions defined on the unit sphere  $\mathbb{S}^2$  and show how diffusion in the frequency domain can be formulated in the spherical setting. All constructions in this

section are finite-dimensional, with a fixed band limit  $L$ ; asymptotic regimes as  $L \rightarrow \infty$  are left for future work.

To this end, we first derive a matrix representation of the spherical discrete Fourier transform, and then use it to define forward and reverse diffusion processes directly in the spectral domain.

Throughout the remainder of this work, we consider an equiangular sampling grid on the sphere as in [28], consisting of  $N_\theta \cdot N_\phi$  points, where

$$N_\theta = 2L, \quad N_\phi = 2L - 1,$$

denote the numbers of colatitude and longitude samples, respectively.

We work with samples of a real-valued spherical signal arranged in vector form as

$$\mathbf{x}^\top = (f(\theta_0, \phi_0), f(\theta_0, \phi_1), \dots, f(\theta_{N_\theta-1}, \phi_{N_\phi-1}))^\top, \quad \mathbf{x} \in \mathbb{R}^{N_\theta N_\phi}.$$

The corresponding vector of reconstructed spherical harmonic coefficients is denoted by

$$\hat{\mathbf{a}}^\top = (\hat{a}_{0,0}, \hat{a}_{1,0}, \hat{a}_{1,1}, \hat{a}_{1,-1}, \hat{a}_{2,0}, \hat{a}_{2,1}, \hat{a}_{2,-1}, \hat{a}_{2,2}, \dots, \hat{a}_{L-1,-L+1}), \quad \hat{\mathbf{a}} \in \mathbb{C}^{L^2}. \quad (6)$$

Finally, we denote by

$$d_X = N_\theta N_\phi = 2L(2L - 1) \quad \text{and} \quad \hat{d}_X = \sum_{\ell=0}^{L-1} (2\ell + 1) = L^2,$$

the dimensions of the spatial and spectral representations, respectively.

**3.1. Matrix expression for the spherical DFT.** The crucial point is that the spherical discrete Fourier transform (DFT),  $\hat{\mathbf{a}} = \mathcal{F}[\mathbf{x}]$ , is *linear* with respect to the sampled signal  $\mathbf{x}$ . This linearity allows the transform to be represented as a matrix operator acting on the vector of spatial samples.

To make this representation explicit, we introduce two matrices associated with the spherical DFT: a full complex matrix  $Y$ , collecting the values of the spherical harmonics evaluated on the sampling grid, and a diagonal matrix  $Q$ , encoding the quadrature weights required for exact integration of  $L$ -band-limited functions on the sphere (see Section 2).

To keep the notation concise, from now on and until the end of this section we adopt the following analysis formula:

$$\hat{a}_{\ell,m} = \sum_{j=0}^{2L-1} \sum_{k=0}^{2L-2} q_j^{(L)} f(\theta_j, \phi_k) Y_{\ell m}^*(\theta_j, \phi_k), \quad (7)$$

which expresses each spectral coefficient as a weighted inner product between the sampled field and the corresponding spherical harmonic. The quadrature weights are given by

$$q_j^{(L)} = \frac{2\pi}{2L-1} \frac{2}{L} \sin \theta_j \sum_{\ell=0}^{L-1} \frac{1}{2\ell+1} \sin((2\ell+1)\theta_j) \quad \text{for } j = 0, \dots, 2L-1.$$

Compared to the standard formulation, the prefactor  $\frac{2\pi}{2L-1}$  has been absorbed into the definition of the quadrature weights, so that the remaining expressions take a compact matrix form.

**Definition 3.1** (Spherical harmonics matrix). Let  $f \in L^2(\mathbb{S}^2)$  be  $L$ -band-limited, and let  $f(\theta_j, \phi_k)$  denote its samples for  $j = 0, \dots, N_\theta - 1$  and  $k = 0, \dots, N_\phi - 1$ . The spherical harmonics matrix  $Y \in \mathbb{C}^{d_X \times \hat{d}_X}$  is defined component-wise by

$$[Y]_{(j,k),(\ell,m)} = Y_{\ell m}(\theta_j, \phi_k).$$

The matrix  $Y$  collects all spherical harmonics up to degree  $L - 1$  evaluated at the sampling locations. Columns correspond to spectral modes  $(\ell, m)$ , according to the same order of coefficients in (6), while rows correspond to spatial grid points  $(\theta_j, \phi_k)$ . This matrix plays the role of a spherical analogue of the Fourier matrix in the Euclidean DFT.

**Definition 3.2** (Sample weights matrix). Under the assumptions of Definition 3.1, let

$$Q_\theta = \text{diag}(q_0, q_1, \dots, q_{N_\theta-1}) \in \mathbb{R}^{N_\theta \times N_\theta}.$$

The sample weights matrix  $Q \in \mathbb{R}^{d_X \times d_X}$  is defined by

$$Q = Q_\theta \otimes I_{N_\phi}, \quad (8)$$

where  $\otimes$  denotes the Kronecker product and  $I_{N_\phi}$  is the identity matrix of size  $N_\phi = 2L - 1$ .

The Kronecker structure reflects the fact that the quadrature weights depend only on the colatitude index  $j$ , while sampling along the longitude direction is uniform.

We are now ready to derive an equivalent matrix–vector representation of the spherical DFT.

**Lemma 3.3** (DFT of a real-valued spherical map). *Let  $f \in L^2(\mathbb{S}^2)$  be  $L$ -band-limited, and let*

$$f(\theta_j, \phi_k)_{j=0, \dots, 2L-1, k=0, \dots, 2L-2}$$

*be its samples on the equiangular grid. Define the vector of spatial samples*

$$\mathbf{x}^\top = (f(\theta_0, \phi_0), f(\theta_0, \phi_1), \dots, f(\theta_{2L-1}, \phi_{2L-2})) \in \mathbb{R}^{2L(2L-1)},$$

*and let  $\hat{\mathbf{a}} \in \mathbb{C}^{L^2}$  be the vector of spherical Fourier coefficients ordered as*

$$\hat{\mathbf{a}}^\top = (\hat{a}_{0,0}, \hat{a}_{1,0}, \hat{a}_{1,1}, \hat{a}_{1,-1}, \dots, \hat{a}_{L-1,-L+1}).$$

*Then the discrete spherical Fourier transform can be expressed as the matrix–vector product*

$$\hat{\mathbf{a}} = U \mathbf{x}, \quad \text{with } U := Y^H Q, \quad (9)$$

*where  $Y$  is the spherical harmonics matrix and  $Q$  the sample weights matrix as in Definitions 3.1 and 3.2.*

The proof is available in Section 5

Lemma 3.3 provides the matrix-vector counterpart of the analysis formula given in Equation (4). In this form, the operator  $U$  acts as the spherical Fourier analysis matrix, combining the evaluation of spherical harmonics with the appropriate quadrature weights.

It is equally straightforward to derive the matrix-vector version of the synthesis formula corresponding to Equation (5). Indeed, for any  $L$ -band-limited signal  $\mathbf{x}$  with spectral coefficients  $\hat{\mathbf{a}}$ , one has

$$\mathbf{x} = Y\hat{\mathbf{a}}. \quad (10)$$

At first glance, this might suggest that  $Y$  is the inverse of  $U$ . This conclusion is, however, incorrect. The matrix  $U$  is not square: in fact,

$$U \in \mathbb{C}^{\hat{d}_X \times d_X}, \quad \hat{d}_X = L^2, \quad d_X = 2L(2L - 1),$$

so that  $U$  maps the higher-dimensional spatial representation into the lower-dimensional spectral one.

We now clarify the precise algebraic relationship between the spherical DFT operator  $U$  and the spherical harmonics matrix  $Y$ , and show how exact reconstruction is nevertheless achieved for band-limited signals despite the dimensional mismatch.

**Lemma 3.4** (Pseudoinverse of the spherical DFT operator  $U$ ). *Let  $U \in \mathbb{C}^{\hat{d}_X \times d_X}$  be the spherical DFT operator as defined in Lemma 3.3, let  $Y \in \mathbb{C}^{d_X \times \hat{d}_X}$  be the spherical harmonics matrix (Definition 3.1), and let  $Q \in \mathbb{R}^{d_X \times d_X}$  be the sample weights matrix (Definition 3.2). In the standard  $L$ -band-limited setting,  $d_X = 2L(2L - 1)$  and  $\hat{d}_X = L^2$ . Then:*

- *Right pseudoinverse: The spherical harmonics matrix  $Y$  is a right pseudoinverse of  $U$ ,*

$$UY = I_{\hat{d}_X}. \quad (11)$$

- *Left pseudoinverse: Let  $P := YU$ . Then for any sampled signal  $\mathbf{x} \in \mathbb{R}^{d_X}$ , the following are equivalent:*

- (1)  $\mathbf{x}$  is  $L$ -band limited; that is, there exists  $\hat{\mathbf{a}} \in \mathbb{C}^{\hat{d}_X}$  with  $\mathbf{x} = Y\hat{\mathbf{a}}$ ;
- (2)  $P\mathbf{x} = \mathbf{x}$ .

The proof is given in Section 5

*Remark 3.5.* The left pseudoinverse lemma provides a clear characterization of the band-limited subspace. The implication from band-limited  $\mathbf{x}$  to  $P\mathbf{x} = \mathbf{x}$  corresponds to the usual "analysis then synthesis recovers the signal" identity. Conversely, the implication from  $P\mathbf{x} = \mathbf{x}$  to  $\mathbf{x}$  being band-limited shows that  $P$  acts as the orthogonal projector (with respect to the  $Q$ -weighted inner product  $\langle u, v \rangle_Q = u^H Q v$ ) onto the band-limited subspace  $\text{range}(Y)$ .

Lemma 3.4 shows that the spherical DFT operator  $U$  admits a pseudoinverse and that band-limited signals are precisely characterized by the

projector  $P = YU$ . This immediately implies a fundamental property of  $U$ : it preserves inner products between the band-limited spatial space and the Fourier coefficient space, which we formalize in the following proposition.

**Proposition 3.6** (Isometry between the  $L$ -band limited spherical signal space and the Fourier coefficients space). *Let  $U \in \mathbb{C}^{\hat{d}_X \times d_X}$  be the spherical DFT operator defined in Lemma 3.3. Under the same assumptions as in Lemma 3.4, let  $\langle \cdot, \cdot \rangle_Q$  denote the  $Q$ -weighted inner product, and let*

$$\left( C_{\text{band-limited}}^{d_X}, \langle \cdot, \cdot \rangle_Q \right)$$

*be the space of  $L$ -band limited signals  $\mathbf{x}$ , i.e., signals for which there exists a vector of spherical Fourier coefficients  $\hat{\mathbf{a}} \in \mathbb{C}^{\hat{d}_X}$  such that  $\mathbf{x} = Y\hat{\mathbf{a}}$ .*

*Then the linear operator  $U$  is an isometry between  $\left( C_{\text{band-limited}}^{d_X}, \langle \cdot, \cdot \rangle_Q \right)$  and  $\left( \mathbb{C}^{\hat{d}_X}, \langle \cdot, \cdot \rangle \right)$ .*

Unlike the Euclidean DFT, the spherical DFT is an isometry only after restriction to the band-limited subspace and with respect to a weighted inner product, a distinction that becomes crucial in the stochastic setting. The proof is presented in Section 5.

**3.2. Diffusion SDEs.** Having expressed the Fourier transform for spherical maps in matrix form, we now derive the diffusion SDEs for spherical signals in the frequency domain by applying the spherical DFT operator  $U$  to the forward spatial-domain SDE, Equation (1). Since the forward SDE is driven by a standard Brownian motion  $\mathbf{w}$ , it is crucial to characterize the image of  $\mathbf{w}$  under the spherical DFT operator  $U$ . We begin by formalizing the class of Gaussian processes that naturally arise in this setting.

**Definition 3.7** (Spherical mirrored Brownian motion). A  $\mathbb{C}^{L^2}$ -valued stochastic process  $\mathbf{v}(t)$  is called a *spherical mirrored Brownian motion* if it satisfies:

- conjugate symmetry  $\mathbf{v}_{(\ell,m)} = (-1)^m \mathbf{v}_{(\ell,-m)}^*$ ,
- independent increments,
- covariance structure  $\mathbb{E}[\varphi(\mathbf{v}(t))\varphi(\mathbf{v}(t))^\top] = t \Sigma$ ,

where  $\Sigma$  is the covariance matrix induced by the spherical DFT and  $\varphi$  extracts the independent real degrees of freedom. The increments are independent in time, although the components may be correlated at fixed times.

Although  $\mathbf{v}(t)$  is complex-valued, its effective dimension is  $L^2$ , corresponding to the independent real degrees of freedom extracted by  $\varphi$ .

The following lemma shows that the spherical Fourier transform of a standard real Brownian motion belongs to this class, and provides an explicit characterization of its components and covariance structure.

**Lemma 3.8** (Image of Brownian motion under the spherical DFT). *Let  $\mathbf{x} \in \mathbb{R}^{d_x}$  be samples of a spherical signal with band limit  $L$ , and let  $\mathbf{w}$  be a standard Brownian motion on  $\mathbb{R}^{d_x}$ . Then the transformed process*

$$\mathbf{v} = U\mathbf{w}$$

*is a continuous stochastic process satisfying the following properties:*

(1) *Symmetry. For all multi-indices  $(\ell, m)$ , the components satisfy*

$$\mathbf{v}_{(\ell, m)} = (-1)^m \mathbf{v}_{(\ell, -m)}^*.$$

(2) *Real Brownian motions. For  $0 \leq \ell < L$ , the rescaled components*

$$\mathbf{v}_{(\ell, 0)} / \sqrt{2C_{(\ell, 0), (\ell', 0)}}$$

*are standard real Brownian motions.*

(3) *Complex Brownian motions. For  $0 \leq \ell < L$  and  $0 < m < L$ , the components can be written as*

$$\mathbf{v}_{(\ell, m)} = \sqrt{C_{(\ell, m), (\ell', m')}} \left( \tilde{\mathbf{w}}_{(\ell, m)}^1 + i \tilde{\mathbf{w}}_{(\ell, m)}^2 \right),$$

*where  $\tilde{\mathbf{w}}_{(\ell, m)}^1$  and  $\tilde{\mathbf{w}}_{(\ell, m)}^2$  are independent standard Brownian motions.*

Here, the factor  $C_{(\ell, m), (\ell', m')}$  is defined as

$$C_{(\ell, m), (\ell', m')} := \frac{2L-1}{2} N_{\ell, m} N_{\ell', m'} \sum_{j=0}^{2L-1} q_j^2 P_{\ell, m}(\cos \theta_j) P_{\ell', m'}(\cos \theta_j).$$

Note that  $C_{(\ell, m), (\ell', m')}$  vanishes unless  $m = m'$ , so the covariance structure is block-diagonal with respect to the azimuthal index  $m$ .

Hence,  $\mathbf{v}$  is a spherical mirrored Brownian motion in the sense of Definition 3.7.

In contrast to the Euclidean setting, and analogously to the spectral time-series case studied in [10], the process  $\mathbf{v}$  is no longer a standard Brownian motion due to the redundancy imposed by conjugate symmetry, that is, the symmetry between the pairs of components  $\mathbf{v}_{\ell, m}$  and  $\mathbf{v}_{\ell, -m}$ . Nevertheless, as shown below, it is possible to recover a standard Brownian motion structure by restricting attention to a subset of non-redundant components.

*Remark 3.9* (Densities and scores for constrained spherical Fourier coefficients). We now provide a technical derivation of the density and score on the constrained Fourier coefficient manifold, which underlies the reverse-time SDE, that is introduced below.

As discussed above, the redundancy between certain components of the spherical DFT  $\hat{\mathbf{a}} \in \mathbb{C}^{L^2}$  of  $\mathbf{x} \in \mathbb{R}^{2L(2L-1)}$  must be taken into account to define a valid probability density  $\hat{p}$  for spherical maps in the frequency domain. This redundancy implies that  $\hat{p}$  is naturally defined on the submanifold

$$\mathbb{C}_{\text{constr}}^{L^2} := \{ \hat{\mathbf{a}} = (\hat{a}_{0,0}, \dots, \hat{a}_{L-1,L-1}) \text{ s.t. } \hat{a}_{\ell, m} = (-1)^m \hat{a}_{\ell, -m}^* \} \subset \mathbb{C}^{L^2}.$$

Following [10], we define a coordinate chart  $\varphi : \mathbb{C}_{\text{constr}}^{L^2} \mapsto \mathbb{R}^{L^2}$  by extracting the unconstrained part of  $\hat{\mathbf{a}}$ . Concretely, we concatenate the relevant real and imaginary parts of the spherical DFT with  $m > 0$ :

$$\varphi[\hat{\mathbf{a}}] := \bigoplus_{\ell=0}^{L-1} \left( \Re(a_{\ell,0}), (\Re(a_{\ell,m}), \Im(a_{\ell,m}))_{m=1}^{\ell} \right), \quad (12)$$

where  $\bigoplus$  denotes vector concatenation. The components satisfy

$$a_{\ell,0} = \varphi_{\ell^2}, \quad \Re(a_{\ell,m}) = \varphi_{\ell^2+2m-1}, \quad \Im(a_{\ell,m}) = \varphi_{\ell^2+2m}, \quad m = 1, \dots, \ell.$$

By symmetry,  $\hat{\mathbf{a}}$  can be uniquely reconstructed from  $\varphi[\hat{\mathbf{a}}]$ , defining the inverse map  $\varphi^{-1} : \mathbb{R}^{L^2} \mapsto \mathbb{C}_{\text{constr}}^{L^2}$  as

$$\varphi^{-1}(\mathbf{z}) = \bigoplus_{\ell=0}^{L-1} \left( \mathbf{z}_{\ell^2}, (\mathbf{z}_{\ell^2+2m-1} + i\mathbf{z}_{\ell^2+2m}, (-1)^m (\mathbf{z}_{\ell^2+2m-1} - i\mathbf{z}_{\ell^2+2m}))_{m=1}^{\ell} \right). \quad (13)$$

With this chart, we define a density on the real vector space  $\hat{p}_{\varphi} : \mathbb{R}^{L^2} \mapsto \mathbb{R}^+$  and pull it back to the constrained manifold:

$$\hat{p} := \hat{p}_{\varphi} \circ \varphi.$$

This ensures  $\hat{p}$  depends only on the independent real and imaginary components of  $\hat{\mathbf{a}}$  and respects the mirror symmetry.

Finally, the score  $\hat{\mathbf{s}} : \mathbb{C}_{\text{constr}}^{L^2} \times [0, T] \mapsto \mathbb{C}^{L^2}$  is constructed analogously. First define the real score on  $\mathbb{R}^{L^2}$ :

$$\hat{\mathbf{s}}_{\varphi}(\mathbf{z}, t) = \nabla_{\mathbf{z}} \log \hat{p}_{\varphi,t}(\mathbf{z}), \quad \mathbf{z} \in \mathbb{R}^{L^2}, t \in [0, T],$$

and pull it back to the constrained manifold:

$$\hat{\mathbf{s}}(\hat{\mathbf{a}}, t) := \varphi^{-1}[\hat{\mathbf{s}}_{\varphi}(\varphi(\hat{\mathbf{a}}), t)], \quad \hat{\mathbf{a}} \in \mathbb{C}_{\text{constr}}^{L^2}. \quad (14)$$

This defines a vector field of partial derivatives with respect to the independent real and imaginary parts of  $\hat{\mathbf{a}}$  and is fully consistent with the symmetry constraints. It thus provides the rigorous foundation for the score term appearing in the reverse-time SDE, Equation (16).

Once a probabilistic model and a well-defined score function for complex-valued frequency coefficients have been introduced, we are in a position to formulate diffusion SDEs directly in the spherical Fourier domain. In particular, we leverage Lemma 3.8 to characterize the dynamics of the spherical Fourier coefficients  $\hat{\mathbf{a}}$  as SDEs driven by spherical mirrored Brownian motions.

**Theorem 3.10** (Diffusion process in the frequency domain). *Let  $\mathbf{x}$  be a diffusion process solving Equation (1) and  $G(t) = g(t)I_{\hat{d}_{\mathbf{x}}}$ . Then its spherical Fourier transform  $\hat{\mathbf{a}} = \mathcal{F}[\mathbf{x}]$  satisfies the forward diffusion SDE in the frequency domain:*

$$d\hat{\mathbf{a}} = \hat{\mathbf{f}}(\hat{\mathbf{a}}, t)dt + g(t)d\tilde{\mathbf{v}}, \quad (15)$$

where  $\hat{\mathbf{f}}(\hat{\mathbf{a}}, t) = U\mathbf{f}(Y\hat{\mathbf{a}}, t)$ , and  $\tilde{\mathbf{v}} = U\mathbf{w}$  is a spherical mirrored Brownian motion on  $\mathbb{C}^{L^2}$ .

The associated reverse-time diffusion process is

$$d\hat{\mathbf{a}} = \hat{\mathbf{b}}(\hat{\mathbf{a}}, t)dt + g(t)d\tilde{\mathbf{v}}, \quad (16)$$

where

$$\hat{\mathbf{b}}(\hat{\mathbf{a}}, t) = \hat{\mathbf{f}}(\hat{\mathbf{a}}, t) - g^2(t)\Sigma\hat{\mathbf{s}}(\hat{\mathbf{a}}, t),$$

$\Sigma \in \mathbb{R}^{L^2 \times L^2}$  is the covariance matrix of the spherical mirrored Brownian motion expressed in the real coordinate system induced by  $\varphi$ ,  $dt$  is a negative infinitesimal time step, and  $\tilde{\mathbf{v}}$  is a spherical mirrored Brownian motion on  $\mathbb{C}^{L^2}$  with time running backward from  $T$  to 0.

Theorem 3.10 provides a practical recipe for implementing diffusion models in the frequency domain for spherical signals. The proof is given in Section 5. It shows that the score-based SDE formalism introduced in [35, 36] extends naturally to this setting, with one important modification: the standard Brownian motion driving the diffusion is replaced by a *spherical mirrored Brownian motion*.

*Remark 3.11* (Covariance structure and effective noise normalization). Lemma 3.8 shows that the noise term

$$\tilde{\mathbf{v}}(t) = U\mathbf{w}(t)$$

appearing in Theorem 3.10 is not a standard Brownian motion on  $\mathbb{C}^{L^2}$ , but a centered Gaussian process with nontrivial covariance. More precisely, the covariance operator of  $\varphi(\tilde{\mathbf{v}}(t))$  is given by

$$\mathbb{E}[\varphi(\tilde{\mathbf{v}}(t))\varphi(\tilde{\mathbf{v}}(t))^\top] = t\Sigma, \quad \text{with } \Sigma \in \mathbb{R}^{L^2 \times L^2}.$$

We emphasize that, due to discretization effects induced by the spherical quadrature, the coefficients  $C_{(\ell,m),(\ell',m')}$  entering  $\Sigma$  need not vanish for  $\ell \neq \ell'$ . Consequently, the covariance matrix  $\Sigma$  is block-structured with respect to the index  $m$ , but is in general non-diagonal in  $\ell$ , as can be seen in Fig. 1.

The covariance matrix  $\Sigma$  is defined with respect to the real coordinate system induced by the chart  $\varphi$ , which extracts the independent real degrees of freedom of the spherical Fourier coefficients. With respect to these coordinates, the entries of  $\Sigma$  take the form

$$\Sigma_{(\ell,m),(\ell',m')} = \begin{cases} 2C_{(\ell,0),(\ell',0)}, & m = m' = 0, \\ C_{(\ell,m),(\ell',m')}, & m = m' > 0, \\ 0, & \text{otherwise.} \end{cases} \quad (17)$$

Here, for  $m > 0$ , the real and imaginary parts of  $a_{\ell,m}$  correspond to distinct coordinates that share the same covariance coefficient  $C_{(\ell,m),(\ell',m')}$ .

As a consequence,  $\Sigma$  is a real, symmetric, and positive semidefinite matrix encoding the full covariance structure induced by the spherical harmonic basis, the quadrature scheme, and the conjugate symmetry constraints.

To express the diffusion SDE in the standard score-based form, it is convenient to introduce a matrix  $\Lambda \in \mathbb{R}^{L^2 \times L^2}$  such that

$$\Sigma = \Lambda \Lambda^\top. \quad (18)$$

The factorization (18) is not unique; any fixed choice (for example, a Cholesky factor) is admissible and is kept constant throughout the diffusion process.

With this notation, the noise term admits the representation

$$\varphi[\tilde{\mathbf{v}}(t)] \stackrel{d}{=} \Lambda \tilde{\mathbf{w}}(t),$$

where  $\tilde{\mathbf{w}}$  is a standard Brownian motion on  $\mathbb{R}^{L^2}$ . Consequently, the forward diffusion SDE in the frequency domain may be equivalently written as

$$d\hat{\mathbf{a}} = \hat{\mathbf{f}}(\hat{\mathbf{a}}, t) dt + g(t) \Lambda d\tilde{\mathbf{w}},$$

and the reverse-time drift involves the term

$$g^2(t) \Sigma \hat{\mathbf{s}}(\hat{\mathbf{a}}, t),$$

where the score  $\hat{\mathbf{s}}$  is taken with respect to the law of  $\hat{\mathbf{a}}$  under this non-isotropic noise.

This formulation makes explicit that the only departure from the Euclidean score-based diffusion framework of [36] lies in the covariance structure of the driving noise, which here reflects the spectral symmetries and redundancy inherent to real-valued spherical signals.

*Remark 3.12* (Consistency with reverse-time theory). The forward spatial-domain SDE (1) is a linear diffusion with additive, state-independent noise. Since the spherical DFT operator  $U$  is linear and deterministic, applying  $U$  to the forward SDE yields a forward diffusion process in the frequency domain whose driving noise is the Gaussian process  $\tilde{\mathbf{v}}(t) = U\mathbf{w}(t)$ .

Although  $\tilde{\mathbf{v}}(t)$  takes values in a complex vector space and its natural covariance is given by  $\mathbb{E}[\tilde{\mathbf{v}}(t)\tilde{\mathbf{v}}(t)^H]$ , the diffusion is most conveniently described in the real coordinate system induced by the chart  $\varphi$ , which extracts the independent real degrees of freedom of the spherical Fourier coefficients.

With respect to these real coordinates, the noise process  $\varphi(\tilde{\mathbf{v}}(t))$  has independent increments and deterministic covariance

$$\mathbb{E}[\varphi(\tilde{\mathbf{v}}(t)) \varphi(\tilde{\mathbf{v}}(t))^\top] = t \Sigma,$$

where the matrix  $\Sigma$  is given by (17). The resulting frequency-domain diffusion therefore falls within the class of linear diffusions with possibly degenerate, non-isotropic covariance considered in the reverse-time theory of [1].

Applying Anderson's formula in the real coordinate system defined by  $\varphi$  yields the reverse-time drift correction term  $g^2(t) \Sigma \hat{\mathbf{s}}(\hat{\mathbf{a}}, t)$ .

**3.3. Relationship between Score Matching Losses.** The final step is to define an appropriate loss in both the spatial and frequency domains and examine their relationship.

In the spatial domain, Proposition 3.6 motivates the following score matching objective:

$$\theta^* = \operatorname{argmin}_{\theta \in \Theta} \mathbb{E}_{t, \mathbf{x}(0), \mathbf{x}(t)} [\mathcal{L}_{SM}(s_\theta, s_{t|0}, \mathbf{x}, t)], \quad (19)$$

$$\mathcal{L}_{SM}(s_\theta, s_{t|0}, \mathbf{x}, t) := \|s_\theta(\mathbf{x}, t) - s_{t|0}(\mathbf{x}, t)\|_Q^2, \quad (20)$$

where the  $Q$ -norm  $\|\cdot\|_Q$  accounts for the spherical topology.

In the frequency domain, the reverse diffusion process from Equation (16) allows sampling of spherical signals via  $\hat{\mathbf{b}}(\hat{\mathbf{a}}, t)$ , which involves the unknown score  $\hat{\mathbf{s}}$ . Analogously, we define an approximating score  $\hat{s}_{\hat{\theta}}$  and optimize the corresponding frequency-domain objective:

$$\begin{aligned} \hat{\theta}^* &= \operatorname{argmin}_{\hat{\theta} \in \Theta} \mathbb{E}_{t, \hat{\mathbf{a}}(0), \hat{\mathbf{a}}(t)} [\mathcal{L}_{SM}(\hat{s}_{\hat{\theta}}, \Sigma \hat{s}_{t|0}, \hat{\mathbf{a}}, t)], \\ \mathcal{L}_{SM}(\hat{s}_{\hat{\theta}}, \Sigma \hat{s}_{t|0}, \hat{\mathbf{a}}, t) &:= \|\hat{s}_{\hat{\theta}}(\hat{\mathbf{a}}, t) - \Sigma \hat{s}_{t|0}(\hat{\mathbf{a}}, t)\|_2^2, \end{aligned} \quad (21)$$

with  $t \sim \mathcal{U}(0, T)$ ,  $\hat{\mathbf{a}}(0) \sim \hat{\mathbf{p}}_0$ ,  $\hat{\mathbf{a}}(t) \sim \hat{\mathbf{p}}_{t|0}(\cdot | \hat{\mathbf{a}}(0))$ , and  $\Sigma$  the matrix from Theorem 3.10. In practice, this involves computing frequency representations of spherical maps, sampling from  $\hat{p}_{t|0}$  via Equation (15), and then mapping the resulting complex signals back to the spatial domain using  $\mathcal{F}^{-1}$ .

A natural question arises: why does minimizing the frequency-domain loss in Equation (21) imply that  $\hat{p}_0 \approx \hat{p}_{\text{data}}$ ? The key idea is to associate to  $\hat{s}_{\hat{\theta}}$  an auxiliary spatial-domain score

$$s'_{\hat{\theta}}(\mathbf{x}, t) := Y \hat{s}_{\hat{\theta}}(U \mathbf{x}, t),$$

where  $Y$  and  $U$  are the isometries from Proposition 3.6. Unlike the Euclidean time-series setting of [10], the spherical geometry and the induced noise covariance prevent an exact equivalence between spatial and frequency domain score matching, leading instead to an inequality that highlights a geometry-induced inductive bias.

**Theorem 3.13** (Score matching losses in spatial and frequency domains). *Let  $\hat{s}_{\hat{\theta}} : \mathbb{C}^{L^2} \times [0, T] \mapsto \mathbb{C}^{L^2}$  satisfy the spherical mirror symmetry  $[\hat{s}_{\hat{\theta}}]_{(\ell, m)} = (-1)^m [\hat{s}_{\hat{\theta}}^*]_{(\ell, -m)}$  for all  $0 \leq \ell < L$  and  $|m| < L$ . Define the auxiliary spatial-domain score  $s'_{\hat{\theta}} : \mathbb{R}^{2L(2L-1)} \times [0, T] \mapsto \mathbb{R}^{2L(2L-1)}$  as above. Then*

$$\begin{aligned} \mathcal{L}_{SM}(\hat{s}_{\hat{\theta}}, \Sigma \hat{s}_{t|0}, \hat{\mathbf{a}}, t) &\leq 2 \left\{ \mathcal{L}_{SM}(s'_{\hat{\theta}}, s_{t|0}, \mathbf{x}, t) \right. \\ &\quad \left. + \|U Z \Sigma \nabla_{\phi[\hat{\mathbf{a}}(t)]} \log p_{t|0}(\phi[\hat{\mathbf{a}}(t)] | \phi[\hat{\mathbf{a}}(0)])\|^2 \right\}, \end{aligned} \quad (22)$$

where

$$\begin{aligned} \hat{s}_{t|0}(\hat{\mathbf{a}}, t) &= \nabla_{\hat{\mathbf{a}}(t)} \log \hat{p}_{t|0}(\hat{\mathbf{a}}(t) | \hat{\mathbf{a}}(0)), \\ s_{t|0}(\mathbf{x}, t) &= \nabla_{\mathbf{x}(t)} \log p_{t|0}(\mathbf{x}(t) | \mathbf{x}(0)), \end{aligned}$$

and  $\Sigma$  is as in Theorem 3.10.

This inequality formalizes a key difference between spherical and Euclidean spectral diffusion: the geometry-induced noise covariance prevents exact equivalence between spatial and frequency score matching, even in the band-limited setting. Unlike [10], where the losses are equivalent, Theorems 3.10 and 3.13 show that the frequency-domain loss is only upper-bounded by the spatial-domain loss. Thus, minimizing the frequency-domain loss does not guarantee convergence to the same optimal score  $s_{\theta^*}$  as in the spatial domain. Instead, it introduces an inductive bias that may affect training dynamics. The next section empirically investigates this effect on the diffusion process. The proof is given in Section 5.

#### 4. NUMERICAL ILLUSTRATIONS

The purpose of this section is to provide illustrative numerical experiments that complement the theoretical analysis developed in the previous sections. Rather than aiming at empirical benchmarking or large-scale performance evaluation, the experiments are designed to validate and visualize the stochastic and geometric effects induced by the spectral formulation of diffusion models on the sphere.

In particular, the numerical results focus on three aspects that play a central role in the theory: (i) the behavior of Brownian motion under the spherical discrete Fourier transform, (ii) the resulting non-isotropic and structured covariance of the driving noise in the frequency domain, and (iii) the practical implications of this geometry-induced noise structure for forward and reverse diffusion dynamics. All experiments are conducted in a finite-dimensional, band-limited setting, consistent with the framework of Section 3.

We first consider synthetic experiments that directly verify the theoretical characterization of the spherical mirrored Brownian motion, by comparing empirical estimates of the covariance matrix with the analytical expression derived in Section 3. These experiments serve as a sanity check of the discrete harmonic analysis and noise transformation underlying the spectral diffusion SDEs.

We then include a learning-based experiment on MNIST-Sphere, a widely used dataset obtained by mapping handwritten digit images onto the sphere. Although the theoretical results of this paper are independent of any specific data distribution, MNIST-Sphere provides a nontrivial and structured test case for spectral diffusion models: it exhibits strong low-frequency spectral bias together with localized, anisotropic spatial features, making it sensitive to the non-isotropic covariance structure induced in the frequency domain. The goal of this experiment is not to claim improved generative performance, but to assess whether the spectral diffusion framework derived in this work remains numerically stable and produces samples of comparable quality when applied to realistic spherical data.

Throughout this section, numerical results should therefore be interpreted as qualitative and diagnostic, rather than as evidence of empirical superiority. They are intended to confirm the theoretical findings, illustrate the impact of geometry on diffusion dynamics, and provide intuition on how spectral diffusion on the sphere departs from its Euclidean counterpart through geometry-induced stochastic structure.

**4.1. Covariance Matrix of the spherical mirrored Brownian motion.** In this section, we report the plot of the covariance matrix  $\Sigma$  of  $\varphi[\tilde{\mathbf{v}}(t)]$  to highlight its particular structure, as defined in Eq. (17).

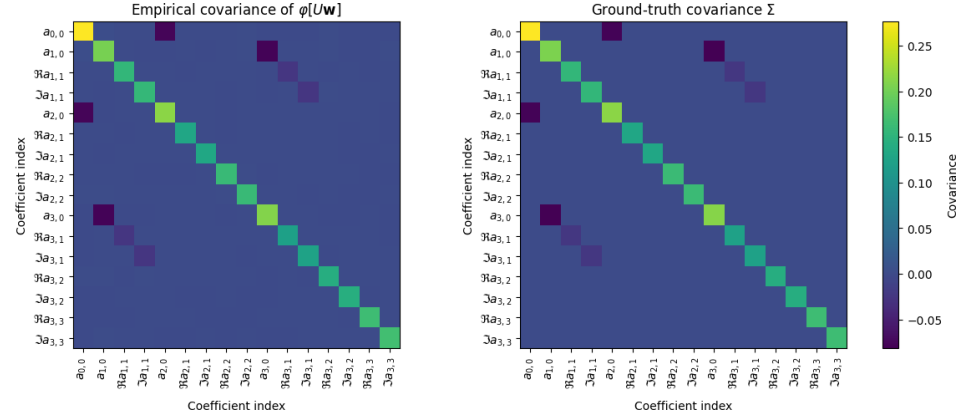


FIGURE 1. Comparison between the empirical covariance matrix of  $\varphi[\tilde{\mathbf{v}}(t)]$ , for  $t = 0$ , estimated from  $5 \times 10^4$  i.i.d samples (left), and the theoretical covariance matrix  $\Sigma$  (right), with maximum bandlimit  $L = 4$ .

**4.2. Model.** For the experimental part, we parametrize the spatial score model  $\mathbf{s}_\theta$  and the frequency score model  $\hat{\mathbf{s}}_{\hat{\theta}}$  as transformer encoders with 10 attention and MLP layers, each with 12 heads and dimension  $d_{\text{model}} = 72$ . Both models have learnable positional encoding as well as diffusion time encoding through random Fourier features composed with a learnable dense layer. This results in a model with approximately 2M parameters. We use a VP-SDE with linear noise scheduling and  $\beta_{\min} = 0.1$  and  $\beta_{\max} = 10$ . The score models are trained with the denoising score-matching loss, as defined in Section 3.3. The model is trained for 200 epochs with batch size 32, AdamW optimizer, and cosine learning rate scheduling (20 warmup epochs,  $lr_{\max} = 10^{-3}$ ).

**4.3. Spatial and Frequency Models.** The essential distinction between spatial-based and frequency-based diffusion models lies in the representation of their input spherical maps. Since all datasets are naturally defined in the

spatial domain, they can be directly processed by the spatial-domain diffusion models  $\mathbf{s}_\theta$ . For the frequency-domain diffusion models  $\hat{\mathbf{s}}_\theta$ , each signal is first transformed into the frequency domain using a Spherical Discrete Fourier Transform (Spherical DFT).

In the spatial domain, the forward and reverse diffusion processes follow the SDEs given in Equations (1) and (2). In the frequency domain, the corresponding forward and reverse processes satisfy the modified SDEs in Equations (15) and (16). The denoised samples  $\hat{\mathbf{x}}(0)$  obtained in the frequency domain can be converted back into the spatial domain by applying the inverse Spherical DFT:  $\hat{x}(0) \mapsto Y\hat{x}(0)$ .

In what follows, we denote by  $S_{\text{spat}} \subset \mathbb{R}^{2L(2L-1)}$  and  $S_{\text{freq}} \subset \mathbb{R}^{L^2}$  the spatial-domain and frequency-domain representations of the samples generated by the respective models. For each model, we generate  $|S_{\text{time}}| = |S_{\text{freq}}| = 1,000$  samples by running the diffusion process for  $T = 1,000$  timesteps.

**4.4. Learning-Based Illustration on MNIST-Sphere.** To complement the synthetic experiments and assess the practical implications of the proposed framework on structured spherical data, we consider a learning-based illustration on MNIST projected onto the unite sphere, which we'll call MNIST-Sphere from here on out. MNIST-Sphere is obtained by mapping handwritten digit images from the MNIST dataset onto the sphere via a fixed spherical projection, following the construction introduced in [9], and resulting in real-valued signals defined on  $\mathbb{S}^2$ . This construction has since become a standard benchmark for spherical generative models. While extrinsic in nature, this dataset is widely used as a controlled testbed for spherical generative models and provides a nontrivial combination of global structure and localized spatial features.

Importantly, MNIST-Sphere exhibits a strongly non-uniform spectral energy distribution, with most of its variance concentrated at low spherical harmonic degrees and pronounced anisotropy in the spatial domain. As a result, it constitutes a challenging test case for diffusion processes driven by non-isotropic and geometry-induced noise in the frequency domain. The purpose of this experiment is not to demonstrate improved generative performance, but to verify that the spectral diffusion SDEs derived in Section 3 remain numerically stable and compatible with learning and sampling on realistic spherical data.

We train two diffusion models with identical architectures and optimization settings: a spatial-domain model operating directly on sampled spherical maps, and a frequency-domain model acting on spherical harmonic coefficients subject to the mirror symmetry constraints described in Section 3.3. Both models are implemented as transformer-based score networks with shared architectural hyperparameters and are trained using denoising score matching under a variance-preserving SDE. All hyperparameters are kept fixed across representations to isolate the effect of the diffusion domain.

In the spatial domain, forward and reverse dynamics follow the standard SDEs in Equations (1) and (2). In the frequency domain, diffusion is governed by the modified SDEs in Equations (15) and (16), where the driving noise has nontrivial covariance  $\Sigma$  induced by the spherical discrete Fourier transform. Samples generated in the frequency domain are mapped back to the spatial domain via the inverse spherical DFT for evaluation.

To compare the distributions induced by the two models, we adopt the *sliced Wasserstein distance* introduced in [4], which provides a computationally tractable proxy for distributional similarity in high-dimensional spaces. With a slight abuse of notation, we denote the sliced Wasserstein distance between two empirical sample sets  $S_1$  and  $S_2$  as  $SW(S_1, S_2)$ . For two distributions  $\mu_1$  and  $\mu_2$ , it is defined as

$$SW_p(\mu_1, \mu_2) := \int_{\mathbb{S}^{d-1}} W_p(P_u \# \mu_1, P_u \# \mu_2) du, \quad (23)$$

where  $\mathbb{S}^{d-1}$  denotes the unit sphere in dimension  $d$ ,  $P_u(x) = u \cdot x$  is the projection of  $x$  onto  $u$ ,  $P_u \# \mu$  is the push-forward of  $\mu$  by  $P_u$ , and  $W_p$  is the Wasserstein distance of order  $p$ . In practice, we approximate (23) via Monte Carlo integration using  $n = 1,000$  random projections and  $p = 2$ :

$$\hat{SW}_p(\mu_1, \mu_2) := \frac{1}{n} \sum_{i=1}^n W_p(P_{u_i} \# \mu_1, P_{u_i} \# \mu_2). \quad (24)$$

Table 1 reports sliced Wasserstein distances as a diagnostic measure of distributional consistency between generated samples and the MNIST-Sphere data distribution, rather than as a competitive performance metric. We stress that sliced Wasserstein distances computed in the spatial and frequency domains live in spaces of different dimensionality; consequently, their absolute values are not directly comparable across metric domains.

TABLE 1. Sliced Wasserstein distances (mean  $\pm$  2 standard errors) between generated samples and the MNIST-Sphere data distribution, computed in both the spatial and frequency domains. Comparable values across diffusion domains indicate that the geometry-induced, non-isotropic noise structure in the frequency-domain SDE does not prevent stable training or sampling, rather than signaling improved generative performance.

Dataset	Metric Domain	Diffusion Domain	
		Frequency	Spatial
MNIST-Sphere	Frequency	$0.0069 \pm 0.0002$	$0.0074 \pm 0.0002$
	Spatial	$0.036 \pm 0.001$	$0.035 \pm 0.001$

*Note:* Absolute values are not directly comparable across metric domains due to the different dimensionalities of the spatial and frequency representations.

Overall, the MNIST-Sphere experiment serves as a robustness check demonstrating that, despite the non-isotropic noise structure and the lack of equivalence between spatial and frequency score matching established theoretically (Theorem 3.13), spectral diffusion on the sphere remains numerically viable and induces sample distributions of comparable quality to its spatial-domain counterpart.

## 5. PROOFS

This section provides detailed proofs of the main results stated in the paper, highlighting the underlying assumptions and key derivations.

*Proof of Lemma 3.3.* Recall that  $Q = Q_\theta \otimes I_{N_\phi}$ , so that in the product  $Y^H Q$  each set of  $N_\phi$  columns corresponding to colatitude  $\theta_j$  is multiplied by the weight  $q_j$ . Then the  $(\ell, m)$ -th entry of the product  $(Y^H Q)\mathbf{x}$  reads

$$[(Y^H Q)\mathbf{x}]_{(\ell, m)} = \sum_{j=0}^{N_\theta-1} \sum_{k=0}^{N_\phi-1} q_j Y_{\ell, m}^*(\theta_j, \phi_k) f(\theta_j, \phi_k),$$

which coincides exactly with the analysis formula for  $\hat{a}_{\ell, m}$ . Hence,  $\hat{\mathbf{a}} = U\mathbf{x}$ , as claimed by Equation 9.  $\square$

*Proof of Lemma 3.4.* We first prove the right pseudoinverse property. By definition,  $U = Y^H Q$ , and the quadrature is exact for  $L$ -band-limited functions. Therefore, we have

$$UY = Y^H QY = I_{L^2}.$$

For the left pseudoinverse, let  $P := YU = YY^H Q$ .

First, assume that  $\mathbf{x}$  is  $L$ -band-limited, meaning  $\mathbf{x} = Y\hat{\mathbf{a}}$  for some  $\hat{\mathbf{a}} \in \mathbb{C}^{L^2}$ . Then

$$P\mathbf{x} = YY^H Q(Y\hat{\mathbf{a}}) = Y(Y^H QY)\hat{\mathbf{a}} = YI_{L^2}\hat{\mathbf{a}} = Y\hat{\mathbf{a}} = \mathbf{x},$$

so  $1 \Rightarrow 2$ .

Conversely, assume that  $P\mathbf{x} = \mathbf{x}$ . By definition, each column of  $P$  is a linear combination of the columns of  $Y$ , so  $\text{range}(P) \subseteq \text{range}(Y)$ . On the other hand, for any  $\mathbf{v} \in \text{range}(Y)$ , we can write  $\mathbf{v} = Y\mathbf{a}$  for some  $\mathbf{a} \in \mathbb{C}^{L^2}$ , and then

$$P\mathbf{v} = YY^H Q(Y\mathbf{a}) = Y(Y^H QY)\mathbf{a} = YI_{L^2}\mathbf{a} = Y\mathbf{a} = \mathbf{v},$$

showing that  $\mathbf{v} \in \text{range}(P)$  and thus  $\text{range}(Y) \subseteq \text{range}(P)$ . We conclude that  $\text{range}(P) = \text{range}(Y)$ . Consequently, if  $P\mathbf{x} = \mathbf{x}$ , then  $\mathbf{x} \in \text{range}(Y)$ , so there exists  $\hat{\mathbf{a}} \in \mathbb{C}^{L^2}$  with  $\mathbf{x} = Y\hat{\mathbf{a}}$ , which shows that  $\mathbf{x}$  is  $L$ -band-limited, which proves the implication  $2 \Rightarrow 1$ .  $\square$

*Proof of Proposition 3.6.* To show that  $U$  is an isometry, we need to prove that it preserves the inner product between the two spaces.

Let  $\mathbf{x}_1, \mathbf{x}_2 \in C_{\text{band-limited}}^{d_X}$ . By definition, there exist  $\hat{\mathbf{a}}_1, \hat{\mathbf{a}}_2 \in \mathbb{C}^{\hat{d}_X}$  such that

$$\mathbf{x}_1 = Y\hat{\mathbf{a}}_1, \quad \mathbf{x}_2 = Y\hat{\mathbf{a}}_2.$$

Then

$$\begin{aligned} \langle U\mathbf{x}_1, U\mathbf{x}_2 \rangle &= (U\mathbf{x}_1)^H (U\mathbf{x}_2) \\ &= \mathbf{x}_1^H U^H U \mathbf{x}_2 \\ &= \mathbf{x}_1^H U^H Y^H Q Y U \mathbf{x}_2 \quad (\text{using the right pseudoinverse: } UY = I_{\hat{d}_X}) \\ &= \hat{\mathbf{a}}_1^H Y^H Q Y \hat{\mathbf{a}}_2 \\ &= \mathbf{x}_1^H Q \mathbf{x}_2 \\ &= \langle \mathbf{x}_1, \mathbf{x}_2 \rangle_Q. \end{aligned}$$

Hence,  $U$  preserves the inner product and is therefore an isometry.  $\square$

*Proof of Lemma 3.8.* We prove each property in turn.

(1) *Symmetry.* This property follows directly from the symmetry of the spherical DFT, which ensures that for all  $(\ell, m)$ ,

$$\mathbf{v}_{(\ell, m)} = (-1)^m \mathbf{v}_{(\ell, -m)}^*.$$

(2) *Real Brownian motions.* Consider the components  $\mathbf{v}_{(\ell, 0)}$ . By symmetry, these are real-valued. To verify that they are standard Brownian motions up to scaling, we first decompose the DFT operator as  $U = U_{re} + iU_{im}$  and compute the covariance structure. Define

$$U_{re}U_{re}^T \quad \text{and} \quad U_{im}U_{im}^T.$$

A direct computation gives

$$[U_{re}U_{re}^T]_{(\ell, 0), (\ell', 0)} = 2C_{(\ell, 0), (\ell', 0)}, \quad [U_{im}U_{im}^T]_{(\ell, 0), (\ell', 0)} = 0, \quad [U_{re}U_{im}^T]_{(\ell, 0), (\ell', 0)} = 0,$$

where

$$C_{(\ell, m), (\ell', m')} := \frac{2L-1}{2} N_{\ell, m} N_{\ell', m'} \sum_{j=0}^{2L-1} q_j^2 P_{\ell, m}(\cos \theta_j) P_{\ell', m'}(\cos \theta_j).$$

Now, for  $s, t \geq 0$  the increment  $\mathbf{v}_{(\ell, 0)}(t+s) - \mathbf{v}_{(\ell, 0)}(s) = U(\mathbf{w}(t+s) - \mathbf{w}(s))$  is Gaussian with mean zero and variance

$$\text{Var}(\mathbf{v}_{(\ell, 0)}(t+s) - \mathbf{v}_{(\ell, 0)}(s)) = t[UU^H]_{(\ell, 0), (\ell, 0)} = t2C_{(\ell, 0), (\ell, 0)}.$$

The continuity and independence of increments follow from the linearity of  $U$  and the corresponding properties of  $\mathbf{w}$ . Hence

$$\mathbf{v}_{(\ell, 0)} / \sqrt{2C_{(\ell, 0), (\ell, 0)}}$$

is a standard real Brownian motion.

(3) *Complex Brownian motions.* Consider  $0 < m < L$ . Decompose  $\mathbf{v}_{(\ell,m)}$  into real and imaginary parts:  $\mathbf{v}_{(\ell,m)} = \Re(\mathbf{v}_{(\ell,m)}) + i\Im(\mathbf{v}_{(\ell,m)})$ . Using the previously computed covariances, we have

$$\begin{aligned}\mathbb{V}\text{ar}(\Re(\mathbf{v}_{(\ell,m)})(t+s) - \Re(\mathbf{v}_{(\ell,m)})(s)) &= tC_{(\ell,m),(\ell,m)}, \\ \mathbb{V}\text{ar}(\Im(\mathbf{v}_{(\ell,m)})(t+s) - \Im(\mathbf{v}_{(\ell,m)})(s)) &= tC_{(\ell,m),(\ell,m)}, \\ \mathbb{C}\text{ov}(\Re(\mathbf{v}_{(\ell,m)}), \Im(\mathbf{v}_{(\ell,m)})) &= 0.\end{aligned}$$

Therefore, the real and imaginary parts are independent standard Brownian motions up to scaling, and we can write

$$\mathbf{v}_{(\ell,m)} = \sqrt{C_{(\ell,m),(\ell,m)}} \left( \tilde{\mathbf{w}}_{(\ell,m)}^1 + i\tilde{\mathbf{w}}_{(\ell,m)}^2 \right),$$

with  $\tilde{\mathbf{w}}_{(\ell,m)}^1$  and  $\tilde{\mathbf{w}}_{(\ell,m)}^2$  independent standard Brownian motions.

This completes the proof.  $\square$

*Proof of Theorem 3.10.* We consider first the *forward SDE*. Since  $\hat{\mathbf{a}} = U\mathbf{x}$  is linear, its Jacobian is  $U$  and its Hessian vanishes. Applying the multivariate Itô's lemma (see [22, Equation (8.3)]), we obtain

$$d\hat{\mathbf{a}} = U\mathbf{f}(\mathbf{x}, t)dt + g(t)Ud\mathbf{w}. \quad (25)$$

By Lemma 3.8,  $\tilde{\mathbf{v}} = U\mathbf{w}$  is a spherical mirrored Brownian motion on  $\mathbb{C}^{L^2}$ , giving the desired forward SDE.

We now consider the *reverse-time SDE*. Following [10], we proceed in three steps:

- (1) define a forward SDE for the truncated coordinates  $\varphi[\hat{\mathbf{a}}]$ ,
- (2) write the associated reverse-time SDE for  $\varphi[\hat{\mathbf{a}}]$ , and
- (3) lift it back to the full process  $\hat{\mathbf{a}}$ .

*Step 1.* Using Equation (15) and Lemma 3.8, the forward SDE for  $\varphi[\hat{\mathbf{a}}]$  reads:

$$d\varphi[\hat{\mathbf{a}}] = \varphi \left[ U\mathbf{f}(Y\varphi^{-1}(\varphi[\hat{\mathbf{a}}]), t) \right] dt + g(t)\Lambda d\tilde{\mathbf{w}}, \quad (26)$$

where

- $\varphi^{-1} : \mathbb{R}^{L^2} \rightarrow \mathbb{C}^{L^2}$  satisfies  $\varphi^{-1}(\varphi[\hat{\mathbf{a}}]) = \hat{\mathbf{a}}$ ,  $\forall \hat{\mathbf{a}} \in \mathbb{C}_{\text{constr}}^{L^2}$ .
- $\Lambda \in \mathbb{R}^{L^2 \times L^2}$  is such that  $\Sigma = \Lambda\Lambda^\top$ , with

$$\Sigma_{(\ell,m),(\ell',m')} = \begin{cases} 2C(\ell, 0; \ell', 0), & m = m' = 0, \\ C(\ell, m; \ell', m), & m = m' > 0, \\ 0, & \text{otherwise,} \end{cases}$$

and  $\tilde{\mathbf{w}}$  is a standard Brownian motion in  $\mathbb{R}^{L^2}$  such that  $\Lambda\tilde{\mathbf{w}} = \varphi[U\mathbf{w}']$ .

*Step 2.* The reverse-time SDE for  $\varphi[\hat{\mathbf{a}}]$  [1] is

$$d\varphi[\hat{\mathbf{a}}] = \left\{ \varphi \left[ U\mathbf{f}(Y\varphi^{-1}(\varphi[\hat{\mathbf{a}}]), t) \right] - g(t)^2 \Lambda \Lambda^\top \nabla_{\varphi[\hat{\mathbf{a}}]} \log \hat{p}_t(\varphi[\hat{\mathbf{a}}]) \right\} dt + g(t)\Lambda d\hat{\mathbf{w}}, \quad (27)$$

with  $\hat{\mathbf{w}}$  a standard Brownian motion in  $\mathbb{R}^{L^2}$ .

*Step 3.* Applying  $\varphi^{-1}$  and using Itô's lemma gives the reverse SDE for  $\hat{\mathbf{a}}$ :

$$\begin{aligned} d\hat{\mathbf{a}} &= \left\{ \varphi^{-1}(\varphi[U\mathbf{f}(Y\hat{\mathbf{a}}, t)]) - g(t)^2 \varphi^{-1}(\Sigma \nabla_{\varphi[\hat{\mathbf{a}}]} \log \hat{p}_t(\varphi[\hat{\mathbf{a}}])) \right\} dt \\ &\quad + g(t) \varphi^{-1}(\Lambda) d\hat{\mathbf{w}}. \end{aligned} \quad (28)$$

where we used that  $\Lambda \Lambda^T = \Sigma$ . Since  $\varphi^{-1}$  is linear, it commutes with deterministic linear operators such as  $\Sigma$ . Therefore, it holds that

$$\Sigma \varphi^{-1}(y) = \varphi^{-1}(\Sigma y)$$

for every  $y \in \mathbb{R}^{L^2}$ . Then, the reverse-time SDE in the  $\hat{\mathbf{a}}$ -coordinates can be written as

$$d\hat{\mathbf{a}} = \left\{ U\mathbf{f}(Y\hat{\mathbf{a}}, t) - g(t)^2 \Sigma \hat{\mathbf{s}}(\hat{\mathbf{a}}, t) \right\} dt + g(t) d\check{\mathbf{v}}, \quad (29)$$

where  $\check{\mathbf{v}} = \varphi^{-1}(\Lambda \hat{\mathbf{w}})$  is a spherical mirrored Brownian motion and  $\hat{\mathbf{s}}$  is the score function defined in Equation (14).  $\square$

*Proof of Theorem 3.13.* The proof proceeds in two steps. *Step 1* establishes preliminary results expressing the score in terms of  $\varphi[\hat{\mathbf{a}}]$ . *Step 2* uses these results to relate the frequency- and spatial-domain score matching losses.

*Step 1: Score in terms of  $\varphi[\hat{\mathbf{a}}]$ .* Since  $\mathbf{x} = Y\varphi^{-1}(\varphi[\hat{\mathbf{a}}])$  with  $\hat{\mathbf{a}} = U\mathbf{x}$ , using the change-of-variable formula yields

$$p_{t|0}(\mathbf{x}(t) | \mathbf{x}(0)) = C \cdot \hat{p}_{t|0}(\varphi[\hat{\mathbf{a}}(t)] | \varphi[\hat{\mathbf{a}}(0)]),$$

where  $C$  is constant because  $\mathbf{x} \mapsto \varphi[U\mathbf{x}]$  is linear. Define  $\varphi[U\mathbf{x}] = VU_{\text{col}}\mathbf{x} = T\mathbf{x}$ , where  $V \in \mathbb{R}^{L^2 \times 2L^2}$ ,  $U_{\text{col}} = \begin{pmatrix} U_{re} \\ U_{im} \end{pmatrix}$ , and  $T \in \mathbb{R}^{L^2 \times 2L(2L-1)}$ .

Note preliminarily that

- For any  $\mathbf{x}$ , it holds that

$$\|U\mathbf{x}\|_2^2 \leq \|\mathbf{x}\|_Q^2. \quad (30)$$

Indeed, let  $A := UQ^{-1/2}$  with  $Q^{-1/2}Q^{-1/2} = Q^{-1}$ . Then

$$\|U\mathbf{x}\|_2^2 = \mathbf{x}^H U^H U \mathbf{x} = (Q^{1/2} \mathbf{x})^H A^H A (Q^{1/2} \mathbf{x}) \leq \lambda_{\max}(A^H A) \|\mathbf{x}\|_Q^2.$$

Using  $U = Y^H Q$ , we obtain  $AA^H = I_{L^2}$ , so  $\lambda_{\max}(A^H A) = 1$ .

- It holds that

$$TT^T = \Sigma \quad (31)$$

This follows from  $U_{\text{col}} U_{\text{col}}^T = \text{diag}(U_{re}^2, U_{im}^2)$ , and  $V$  extracts the relevant truncation indices.

- For any  $\mathbf{y} \in \mathbb{R}^{L^2}$ , it holds that

$$T^T \mathbf{y} = T^+ \Sigma \mathbf{y}, \quad (32)$$

where  $T^+ = T^T (TT^T)^{-1}$  is the Moore-Penrose pseudoinverse. Indeed, to obtain the result, simply multiply both sides of (31) by  $T^+$ . Moreover, also  $Y\varphi^{-1}$  acts as a right pseudoinverse of  $T$ :

$$TY\varphi^{-1}[\mathbf{y}] = \mathbf{y}, \quad \forall \mathbf{y}.$$

So, in general, we can write

$$Y\varphi^{-1} = T^+ + Z, \quad \text{with } TZ = 0. \quad (33)$$

Here  $Z$  collects the components of  $Y\varphi^{-1}$  lying in  $\ker(T)$ .

Using these results, the chain rule gives

$$\nabla_{\mathbf{x}(t)} \log p_{t|0} (\mathbf{x}(t) | \mathbf{x}(0)) = T^\top \nabla_{\varphi[\hat{\mathbf{a}}(t)]} \log \hat{p}_{t|0} (\varphi[\hat{\mathbf{a}}(t)] | \varphi[\hat{\mathbf{a}}(0)]). \quad (34)$$

*Step 2: Bounding the frequency-domain loss.* By Equation (14) and using the triangle inequality  $\|u + v\|_2^2 \leq 2(\|u\|_2^2 + \|v\|_2^2)$ , it holds that

$$\begin{aligned} & \|\hat{s}_{\hat{\theta}}(\hat{\mathbf{a}}, t) - \Sigma \hat{s}_{t|0}(\hat{\mathbf{a}}, t)\|_2^2 \\ &= \|\hat{s}_{\hat{\theta}}(\hat{\mathbf{a}}, t) - \Sigma \varphi^{-1} \nabla_{\varphi[\hat{\mathbf{a}}(t)]} \log \hat{p}_{t|0}\|_2^2 \\ &= \|\hat{s}_{\hat{\theta}}(\hat{\mathbf{a}}, t) - UY\varphi^{-1} (\Sigma \nabla_{\varphi[\hat{\mathbf{a}}(t)]} \log \hat{p}_{t|0})\|_2^2 \\ &= \|\hat{s}_{\hat{\theta}}(\hat{\mathbf{a}}, t) - U(T^+ + Z)\Sigma \nabla_{\varphi[\hat{\mathbf{a}}(t)]} \log \hat{p}_{t|0}\|_2^2 \\ &\leq 2 \left( \|\hat{s}_{\hat{\theta}}(\hat{\mathbf{a}}, t) - UT^+ \Sigma \nabla_{\varphi[\hat{\mathbf{a}}(t)]} \log \hat{p}_{t|0}\|_2^2 + \|UZ\Sigma \nabla_{\varphi[\hat{\mathbf{a}}(t)]} \log \hat{p}_{t|0}\|_2^2 \right). \end{aligned}$$

Note that the appearance of  $\Sigma$  inside the loss (rather than as a metric) reflects the form of the reverse drift induced by the non-isotropic noise.

Finally, the first term can be upper-bounded using Equations (30) and (32), together with the chain rule:

$$\begin{aligned} \|\hat{s}_{\hat{\theta}} - UT^+ \Sigma \nabla_{\varphi[\hat{\mathbf{a}}(t)]} \log \hat{p}_{t|0}\|_2^2 &= \left\| U s'_{\hat{\theta}}(\mathbf{x}, t) - U \nabla_{\mathbf{x}(t)} \log p_{t|0} (\mathbf{x}(t) | \mathbf{x}(0)) \right\|_2^2 \\ &\leq \left\| s'_{\hat{\theta}}(\mathbf{x}, t) - \nabla_{\mathbf{x}(t)} \log p_{t|0} (\mathbf{x}(t) | \mathbf{x}(0)) \right\|_Q^2. \end{aligned}$$

This concludes the proof.  $\square$

## REFERENCES

- [1] B. D. O. Anderson. Reverse time diffusion equation models. *Stochastic Processes and their Applications*, 12:313–326, 1982.
- [2] K. Atkinson and W. Han. *Spherical Harmonics and Approximations on the Unit Sphere: An Introduction*. Springer, 2012.
- [3] P. Baldi, L. Caramellino, and M. Rossi. Large deviations of conditioned diffusions and applications. *Stochastic Processes and their Applications*, 130(3):1289–1308, 2020.
- [4] N. Bonneel, J. Rabin, G. Peyré, and H. Pfister. Sliced and Radon Wasserstein barycenters of measures. *Journal of Mathematical Imaging and Vision*, 51:22–45, 2015.
- [5] A. Caponera, C. Durastanti, and A. Vidotto. Lasso estimation for spherical autoregressive processes. *Stochastic Processes and their Applications*, 137:167–199, 2021.
- [6] A. Caponera and D. Marinucci. Asymptotics for spherical functional autoregressions. *The Annals of Statistics*, 49(1):346–369, 2021.
- [7] J. Carrón Duque and D. Marinucci. Geometric methods for cosmological data on the sphere. *Annual Review of Statistics and Its Application*, 11:437–460, 2024.
- [8] N.R. Cavanaugh, T.A. O'Brien, W.D. Collins, and W.C. Skamarock. Spherical harmonic spectral estimation on arbitrary grids. *Monthly Weather Review*, 145(8):3355–3363, 2017.

- [9] B. Coors, A.P. Condurache, and A. Geiger. Spherenet: Learning spherical representations for detection and classification in omnidirectional images. In *Computer Vision – ECCV 2018: 15th European Conference, Munich, Germany, September 8–14, 2018, Proceedings, Part IX*, pages 525–541, 2018.
- [10] J. Crabbé, N. Huynh, J. Stanczuk, and M. Van Der Schaar. Time series diffusion in the frequency domain. In *Proceedings of the 41st International Conference on Machine Learning (ICML 2024)*, pages 1–32. JMLR.org, 2024.
- [11] V. De Bortoli, É. Mathieu, M. Hutchinson, J. Thornton, Y. W. Teh, and A. Doucet. Riemannian score-based generative modelling. In *Advances in Neural Information Processing Systems*, volume 35, pages 2406–2422. Curran Associates, Inc., 2022.
- [12] P. Dhariwal and A. Nichol. Diffusion models beat gans on image synthesis. *Advances in Neural Information Processing Systems*, 34:8780–8794, 2021.
- [13] S. Dieleman, L. Sartran, A. Roshannai, N. Savinov, Y. Ganin, P.H. Richemond, A. Doucet, R. Strudel, C. Dyer, and C. Durkan. Continuous diffusion for categorical data. arXiv:2211.15089, 2022.
- [14] H. Ding, S. Fang, and X.-D. Li. Stochastic parallel translations and diffusions on the Wasserstein space. *Stochastic Processes and their Applications*, 184:104602, 2025.
- [15] J.R. Driscoll and D.M. py. Computing fourier transforms and convolutions on the 2-sphere. *Advances in Applied Mathematics*, 15(2):202–250, 1994.
- [16] C. Durastanti. Aliasing effects for samples of spin random fields on the sphere. *Journal of Fourier Analysis and Applications*, 2026. to appear.
- [17] C. Durastanti, X. Lan, and D. Marinucci. Gaussian semiparametric estimates on the unit sphere. *Bernoulli*, 20(1):28–77, 2014.
- [18] C. Durastanti and T. Patschkowski. Aliasing effects for random fields over spheres of arbitrary dimension. *Electronic Journal of Statistics*, 13:3297–3335, 2019.
- [19] J. Ho, A. Jain, and P. Abbeel. Denoising diffusion probabilistic models. In *Advances in Neural Information Processing Systems*, volume 33, pages 6840–6851. Curran Associates, Inc., 2020.
- [20] A. Hyvärinen. Estimation of non-normalized statistical models by score matching. *Journal of Machine Learning Research*, 6:695–709, 2005.
- [21] T. Karras, S. Laine, M. Aittala, J. Hellsten, J. Lehtinen, and T. Aila. Analyzing and improving the image quality of stylegan. In *2020 IEEE/CVF Conference on Computer Vision and Pattern Recognition (CVPR), Seattle, WA, USA, June 13–19, 2020*, pages 8107–8116. Computer Vision Foundation / IEEE, 2020.
- [22] P. E. Kloeden and E. Platen. *Numerical Solution of Stochastic Differential Equations*, volume 23 of *Applications of Mathematics*. Springer-Verlag, 1992.
- [23] Z. Kong, W. Ping, Y. Chen, and B. Catanzaro. Diffwave: A versatile diffusion model for audio synthesis. In *Proceedings of the International Conference on Machine Learning (ICML)*, 09 2020.
- [24] T.-H. Li and G.R. North. Aliasing effects and sampling theorems of spherical random fields when sampled on a finite grid. *Annals of the Institute of Statistical Mathematics*, 49:341–354, 1997.
- [25] N. Mahmoudian Bidgoli, R.G. de Azevedo, T. Maugey, A. Roumy, and P. Frossard. Oslo: On-the-sphere learning for omnidirectional images and its application to 360-degree image compression. *IEEE Transactions on Image Processing*, 31:5813–5827, 2022.
- [26] L. Mak, S. Grandison, and R.J. Morris. An extension of spherical harmonics to region-based rotationally invariant descriptors for molecular shape description and comparison. *Journal of Molecular Graphics and Modelling*, 26(7):1035–1045, 2008.
- [27] D. Marinucci and G. Peccati. *Random Fields on the Sphere: Representation, Limit Theorems and Cosmological Applications*. Cambridge University Press, 2011.
- [28] J. McEwen and Y. Wiaux. A novel sampling theorem on the sphere. *Signal Processing, IEEE Transactions on*, 59:5876 – 5887, 01 2012.

- [29] E. Mirafzali, U. Gupta, P. Wyrod, F. Proksa, D. Venturi, and R. Marinescu. Malliavin-Bismut score-based diffusion models. arXiv:2503.16917, 2025.
- [30] N. Perraudin, Defferrard M., T. Kacprzak, and R. Sgier. DeepSphere: Efficient spherical convolutional neural network with HEALpix sampling for cosmological applications. *Astronomy and Computing*, 27:130–146, 2019.
- [31] C. Saharia, J. Ho, W. Chan, T. Salimans, D.J. Fleet, and M. Norouzi. Image super-resolution via iterative refinement. *IEEE Transactions on Pattern Analysis and Machine Intelligence*, 45(4):4713–4726, 2022.
- [32] P. J. Schreier and L. L. Scharf. *Statistical Signal Processing of Complex-Valued Data: The Theory of Improper and Noncircular Signals*. Cambridge University Press, 2010.
- [33] J. Sohl-Dickstein, E. Weiss, N. Maheswaranathan, and S. Ganguli. Deep unsupervised learning using nonequilibrium thermodynamics. In *Proceedings of the International Conference on Machine Learning (ICML)*, pages 2256–2265. PMLR, 2015.
- [34] Y. Song and S. Ermon. Generative modeling by estimating gradients of the data distribution. In *Advances in Neural Information Processing Systems*, volume 32, 2019.
- [35] Y. Song and S. Ermon. Improved techniques for training score-based generative models. In H. Larochelle, M. Ranzato, R. Hadsell, M.F. Balcan, and H. Lin, editors, *Advances in Neural Information Processing Systems*, volume 33, pages 12438–12448. Curran Associates, Inc., 2020.
- [36] Y. Song, J. Sohl-Dickstein, D.P. Kingma, A. Kumar, S. Ermon, and B. Poole. Score-based generative modeling through stochastic differential equations. In *International Conference on Learning Representations (ICLR) 2020*, 2020.
- [37] G. Szegö. *Orthogonal Polynomials*. American Mathematical Society, 1975.
- [38] W. Tang and H. Zhao. Score-based diffusion models via stochastic differential equations. *Statistical Surveys*, 19:28–64, 2025.
- [39] M. Uz, O. Akyilmaz, C.K. Shum, K.G. Atman, S. Olgun, and Ö. Günes. High-resolution temporal gravity field data products: Monthly mass grids and spherical harmonics from 1994 to 2021. *Scientific Data*, 11:71, 2024.
- [40] Q. Wang, K. Birod, C. Angioni, S. Grösch, T. Geppert, P. Schneider, M. Rupp, and G. Schneider. Spherical harmonics coefficients for ligand-based virtual screening of cyclooxygenase inhibitors. *PloS One*, 6:e21554, 2011.
- [41] J.L. Watson, D. Juergens, N.R. Bennett, B.L. Trippe, J. Yim, H.E. Eisenach, W. Ahern, A.J. Borst, R.J. Ragotte, and L.F. Milles. De novo design of protein structure and function with rfdiffusion. *Nature*, 620(7976):1089–1100, 2023.
- [42] M. Xu, L. Yu, Y. Song, C. Shi, S. Ermon, and J. Tang. Geodiff: A geometric diffusion model for molecular conformation generation. In *Proceedings of the International Conference on Learning Representations (ICLR) 2022*, 2022.
- [43] C. Zeni, R. Pinsler, D. Züigner, A. Fowler, M. Horton, X. Fu, Z. Wang, A. Shysheya, J. Crabbé, S. Ueda, R. Sordillo, L. Sun, J. Smith, B. Nguyen, H. Schulz, S. Lewis, C.-W. Huang, Z. Lu, Y. Zhou, H. Yang, H. Hao, J. Li, C. Yang, W. Li, R. Tomioka, and T. Xie. A generative model for inorganic materials design. *Nature*, 639(8055):624–632, 2025.

DEPARTMENT OF STATISTICAL SCIENCES, SAPIENZA UNIVERSITY OF ROME, ITALY  
*Email address:* pierpaolo.brutti@uniroma1.it

DEPARTMENT OF BASIC AND APPLIED SCIENCES FOR ENGINEERING, SAPIENZA UNIVERSITY OF ROME, ITALY  
*Email address:* claudio.durastanti@uniroma1.it

DEPARTMENT OF STATISTICAL SCIENCES, SAPIENZA UNIVERSITY OF ROME, ITALY  
*Email address:* francesco.mari@uniroma1.it